Numerical modeling of pile response in soft clay under multidirectional and cyclic loading for floating wind turbines

Cristian Soriano, Luc Thorel, Matthieu Blanc, Hans Peter Jostad

Numerical Modeling of Pile Response in Soft Clay under Multidirectional and Cyclic Loading for Floating Wind Turbines

Cristian Soriano[1*], Luc Thorel[1], Matthieu Blanc[1], Hans Peter Jostad[2]

[1] GERS - Geotechnical Centrifuge CG, Université Gustave Eiffel,

Allée des Ponts et Chaussées, Bouguenais, F-44344, France.

[2] Advanced Modelling Department, Norwegian Geotechnical Institute,

Sandakerveien 140, Oslo, 0484, Norway.

* Corresponding author(s). Email(s):

cristian.soriano-camelo@univ-eiffel.fr

Contributing authors: luc.thorel@univ-eiffel.fr; matthieu.blanc@univ-eiffel.fr; Hans.Petter.Jostad@ngi.no

Abstract

Floating wind turbines offer a competitive advantage for harvesting renewable energy, particularly in locations with abundant wind resources. Among the critical components of these systems, anchoring and mooring systems are required to secure the wind turbines in place. Pile anchors are among the anchoring solutions currently available for floating wind turbines. Consequently, this study focuses on the behavior of pile anchors installed in soft clay subjected to cyclic loading, including multidirectional forces. To investigate this, a numerical model was developed via OpenSees and calibrated based on existing centrifuge test data. The results demonstrate that non-symmetrical cyclic loads induce the most significant accumulation of permanent pile displacements compared with two-way cyclic loading. Conversely, load reversals can contribute to a reduction in these displacements. Finally, the use of an axisymmetric anchor configuration appears beneficial for resisting complex loading patterns typical of floating wind turbines, as it can promote a more uniform mobilization of the pile's holding capacity.

Keywords: Offshore wind farms, multiline anchors, cyclic loading, clay

1. Introduction

Offshore wind farms are rapidly expanding into deep water locations (>60 m depth) to access areas with high wind resources and mitigate impacts on the shoreline (Lee et al., 2020; Rezaei et al., 2023). This trend has driven the expansion of floating wind turbines (FOWTs) due to their flexibility in terms of size and reduced landscape impacts compared with fixed installations (OWTs) (Brussa et al., 2023). With this increased demand for FOWTs, various platform designs have been developed, categorized into four types: spar, barge, semi-submersible and tension leg platforms (Edwards et al., 2023). These developments necessitate the study of suitable mooring and anchoring systems for future FOWTs. The solutions, adapted from the oil and gas industry to the floating wind industry, encompass several types of anchors including driven piles, suction embedded plate anchors (SEPLAs), suction caissons, dynamically embedded plate anchors (DEPLAs), and drag embedded anchors (Aubeny, 2017; Cerfontaine et al., 2023).

A shared characteristic among all anchor types is the complex cyclic loads transferred from the wind turbine floaters via the mooring lines. These loads, characterized by a sustained component and interactions with wind, wave, and current components (WWC), can lead to significant anchor displacements and a reduction in soil shear strength due to soil structure breakdown (Andersen, 2015; Aubeny, 2017). This ongoing degradation can ultimately compromise the anchor's integrity and the overall stability of the floating wind unit (Hallowell et al., 2018).

Numerical and physical modeling have been used to study the behavior of offshore anchors under monotonic, cyclic, and multidirectional loading. Regarding numerical studies, Gogoi et al. (2023) investigated the performance of multiline ring anchors in sandy soils under monotonic loading conditions via 3D finite element modeling. Al-Janabi and Aubeny (2022) addressed the performance of piles and suction caissons subjected to cyclic loading to observe the accumulation of displacements of this type of anchors when installed in clayey soils. Kwa et al. (2023) developed anchor macroelement models that couple the anchor, mooring line and floater as a system. Cerfontaine et al. (2019) conducted a numerical study to determine the uplift resistance and identify the failure mechanisms of shallow plate and screw anchors. Yan et al. (2024) investigated the bearing capacity of shared anchors in sand under multidirectional loading, including factors such as the load angle and soil density. In terms of physical modelling research projects, Chung (2012) and Burns et al. (2014) conducted centrifuge tests to investigate the behavior of suction caissons installed in clay under inclined and cyclic orthogonal loads to simulate the arrival of two mooring lines (2-line) to a single anchor. Spicer et al. (2022) performed 1-g tests to study the performance of anchor piles in sand subjected to loads representative of tension leg platforms to integrate the framework of stability diagrams in the design of this type of anchors. Herduin (2019) investigated the behavior of pile and suction anchors in sand under multidirectional loading providing extensive datasets of displacements and rotations for 2-line and 3-line anchor configurations.

Despite these advancements, a gap remains in understanding the combined effects of different load characteristics (average and cyclic components, directionality) and complex loading scenarios (multidirectional) on pile response in soft clay. This study focuses on the response of piles in soft clay subjected to various load scenarios. For this purpose, a numerical modeling approach was developed in OpenSees software (McKenna et al., 2004) by incorporating the pressure-independent multiyield (PIMY) soil constitutive model. This model uses a nonlinear backbone curve and a multi-surface plasticity framework to simulate cyclic soil behavior. While the PIMY model captures stiffness degradation implicitly through hysteretic response and strain accumulation, it does not account for the cyclic degradation of the undrained shear strength or the onset of cyclic failure due to pore pressure buildup, as it follows a total stress formulation. Nevertheless, its relative simplicity and computational efficiency make it suitable for exploring general trends in displacement accumulation under multidirectional loading. The model performance was evaluated through comparisons with centrifuge test data involving monotonic and cyclic load scenarios.

Following the calibration of the numerical model, a parametric study was conducted to explore the influence of various load characteristics on the pile response. This study investigates the effects of average and cyclic load components (non-symmetric cyclic loading), load directionality (unidirectional and multidirectional), and varying load amplitudes. The multidirectional loading scenarios simulate the complex loads experienced by pile anchors in multiline systems (shared anchors). The findings of this study aim to shed light on the factors influencing the cyclic behavior of offshore piles in soft clay, particularly in terms of the development of cyclic and permanent displacements when loaded. Although this study does not focus primarily on load capacity, it provides a numerical modeling framework that describes cyclic displacements of piles in clay including complex load scenarios such as those that can be encountered in the application of the shared anchors concept for floating wind turbines.

This study addresses the limited understanding of pile anchor response in soft clay under realistic, multidirectional cyclic loading conditions relevant to FOWTs with shared anchors. The novelty lies in the application of time histories derived from representative wind, wave, and current conditions to simulate loading paths that extend beyond idealized cyclic patterns. A simplified numerical model is implemented in OpenSees, using a total stress formulation with known limitations, to capture key trends in cyclic displacement accumulation. A practical contribution of this work is the introduction of a procedure for applying load multipliers under multidirectional conditions, which can be adapted for use in other finite element software. While the approach is based on a simplified constitutive model, it provides a framework that can be extended for more advanced modeling and supports future studies involving more complex soil behavior and validation.

2. Numerical Modeling Approach

The numerical modeling approach in this study involved calibrating a pile model based on centrifuge experiments, followed by a series of parametric analyses.

2.1 Baseline model: SOLCYP centrifuge test

As a baseline for the calibration of the numerical models developed in this research, a set of centrifuge tests conducted at the Université Gustave Eiffel (formerly IFSTTAR) were utilized (Khemakhem et al., 2010; Khemakhem et al., 2012a; Khemakhem et al., 2012b). These tests, conducted under the framework of the SOLCYP project (Puech and Garnier, 2017), involved piles installed in kaolin clay and subjected to both monotonic loading and cyclic loading. The centrifuge experiments were performed at a centrifugal acceleration of n=50 g. Figure 1 shows the geometric parameters of the pile, and Table 1 summarizes the model and prototype dimensions of the reference model and the scaling laws that link the behavior between the model and the prototype (Garnier et al., 2007). In these scaling laws, 'n' is the geometric scaling factor, which corresponds to the centrifugal acceleration level (n = 50).

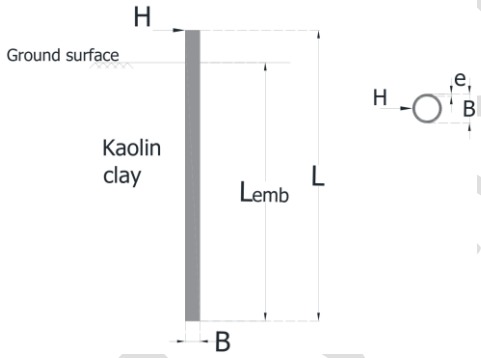

Fig.1. Pile geometry parameters

Table 1. Pile geometry parameters at the model and prototype scales

Parameter	Model dimensions	Scaling law model/prototype	Prototype dimensions
Length, L	360 mm	1/n	18 m
Embedded length, L_{emb}	320 mm	1/n	16 m
Diameter, B	18 mm	1/n	0.954 m*
Wall thickness, e	1 mm	1/n	40 mm**
Modulus of elasticity, E_p	74 GPa (aluminum)	1	74 GPa (aluminum)
Flexural rigidity, E_pI_p	—	—	895 MN•m^2

* The pile diameter was increased by 6% due to silicon resin to protect the pile instrumentation.
** The pile wall thickness was adjusted to achieve the target flexural rigidity.

The model pile was installed at 1 g in a pre-bored hole with a smaller diameter. This installation method can be categorized as "wished-in-place". For the measurement of bending moments within the pile during the centrifuge experiments, a total of 21 levels of strain gauges were installed. To ensure waterproofing, the strain gauges on the instrumented piles were protected by a flexible silicone resin. This coating increased the external diameter of the pile by approximately 6%. Owing to the flexible nature of the resin, its contribution to the overall bending stiffness (E_pI_p) of the pile was considered

negligible, and the calibrated stiffness of the base aluminum section was used for calculating the bending moments. However, to correctly model the soil-pile interaction, all subsequent analyses, including the derivation of p-y curves, were conducted using the effective external diameter of the coated pile (0.954 m at the prototype scale). Additionally, the wall thickness was adjusted to achieve a target flexural rigidity for the prototype pile, equivalent to 895 MN•m^2 as reported by Khemakhem (2012a). The point of application for the monotonic and cyclic loads was positioned at the pile head, located 2 m above ground level.

To determine the behavior of the pile in terms of its relative stiffness to the soil (flexible, semi-flexible, or rigid), the criterion of Poulos and Hull (1989) was employed. The pile-soil relative stiffness was calculated as $E_pI_p/E_sL_{emb}^4$, where E_p is the pile Young's modulus, I_p is the pile moment of inertia, E_s is the soil Young's modulus and L_{emb} is the embedded length of the pile. This equation has upper and lower boundary values of 0.0025 and 0.208, corresponding to flexible and rigid piles, respectively. For simplicity, E_s was taken as the average Young's modulus over the upper half of the pile, where the highest bending moments and shear stresses typically occur. Based on the provided information ($E_pI_p = 895MN \cdot m^2$, $L_{emb} = 16\,m$, $E_s = 1.6\,MPa$ as reported by Khemakhem, 2012a), the stiffness ratio for the model was estimated to be 0.0085 classifying it as a semi-rigid pile.

2.2 Soil profile

The soil profile utilized for calibrating the numerical model comprised slightly overconsolidated kaolin clay. The model preparation involved a reconstitution method, consisting of mixing dry Speswhite kaolin clay powder with water to create a slurry with a water content of 90%. The basic physical and mechanical properties of the Speswhite kaolin clay used are summarized in Table 2.

Table 2. Properties of Speswhite kaolin clay (Lau, 2015)

Property	Value
Plastic limit, PL (%)	30
Liquid limit, LL (%)	63
Plasticity index, PI (%)	33
Specific gravity, G_s	2.60
Slope of critical state line (CSL)	0.90
Slope of unload-reload line, κ	0.039
Intercept of CSL at mean effective stress p'=1 kPa, Γ	3.31
Slope of normal consolidation line, λ	0.22

The clay was then consolidated inside a cylindrical model container in three distinct sublayers, each subjected to a sequence of consolidation pressures at 1 g via a hydraulic press. A subsequent phase of consolidation occurred in the centrifuge at 50 g for 4 hours (at the model scale). Four piles were installed in the model container and positioned to ensure a minimum spacing of 10 times the pile diameter

between them. In-flight cone penetration tests (CPTs) were conducted to determine the undrained shear strength (s_u) of the clay. For this study, the potential effects of strength anisotropy were not considered, and the undrained shear strength derived from CPT tests was assumed to be isotropic. Figure 2 presents the layout of one centrifuge experiment, showing the pile locations within the container, the axis along which CPTs were performed, and the corresponding experimental and linear undrained shear strength profiles. Based on the experimental results, Khemakhem (2012a) proposed an undrained shear strength profile as a function of depth (z, in meters):

$$s_u = 1.27 + 1.17z \quad [kPa] \tag{1}$$

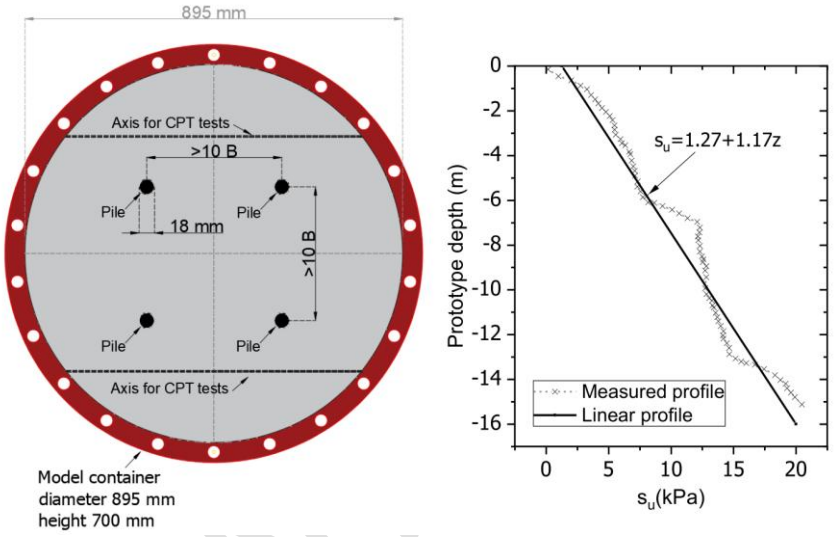

Fig.2. Slightly overconsolidated clay: Experimental layout and measured versus linear undrained shear strength profiles (adapted from Khemakhem, 2012a)

2.3 Finite-element Model Calibration

The numerical model employed in this research was developed using OpenSees v3.5.0 (McKenna et al., 2000). A 3D nonlinear model of the pile and the surrounding soil was constructed using 8-node brick elements with reduced integration to improve computational performance and mitigate locking. The pile was simulated by the '*elasticBeamColumn*' element type, characterized by its Young's modulus (E), moment of inertia (I) and mass density(ρ).

The soil was modeled as a nonlinear hysteretic material utilizing a Von Mises multi-surface kinematic plasticity model, designated '*PressureIndependentMultiYield*' (PIMY) (Yang et al., 2003). The PIMY model is capable of simulating both monotonic and cyclic responses of materials, particularly those with shear behavior insensitive to confinement changes, such as clay loaded under undrained conditions. The model incorporates nested yield surfaces (denoted as f_1, f_M, ... f_{NYS} in the deviatoric plane in Figure 3) to control the plastic modulus. This feature allows the model to be calibrated to a

predetermined stress-strain response, known as a backbone curve. This backbone curve, which defines the nonlinear shear stress-strain relationship, is approximated by a hyperbolic function (Kondner, 1963):

$$\tau = \frac{G\gamma}{1 + {}^{\gamma}/_{\gamma_r}} \tag{2}$$

where τ and γ represent the octahedral shear stress and shear strain, respectively. G is the low-shear strain modulus. γ_r is a reference shear strain defined as:

$$\gamma_r = \frac{\gamma_{max} * \tau_{max}}{G\,(\gamma_{max} - \tau_{\max})} \tag{3}$$

where τ_{max} refers to the shear strength achieved at large shear strains (i.e., $\tau_{max} \approx \tau$ at $\gamma \rightarrow \infty$). The PIMY material exhibits linear elastic behavior during the application of gravity loading. Under dynamic conditions, the stress-strain response is governed by the multi-surface plasticity framework, where the material follows an associative flow rule.

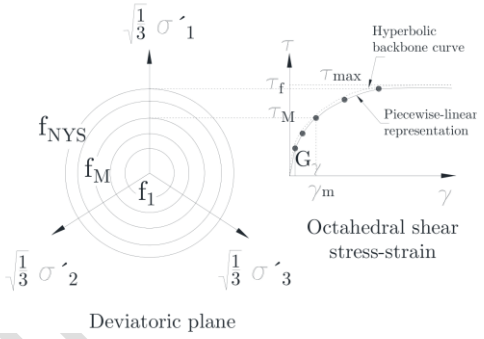

Fig. 3. Hyperbolic backbone curve for the nonlinear shear stress-strain response in multisurface plasticity (Prevost, 1985)

The PIMY model is a total-stress, pressure-independent formulation that does not incorporate explicit mechanisms for the cyclic degradation of shear strength or stiffness. Instead, cyclic behavior arises implicitly from the multi-surface plasticity framework and the shape of the hyperbolic backbone curve. The accumulation of permanent strain during cyclic loading—commonly referred to as ratcheting—is not controlled by direct input parameters but emerges from the implementation of a Mroz-type kinematic hardening rule (Mroz, 1967; Prevost, 1985). While this approach captures cyclic hysteresis and stiffness reduction to some extent, the model does not simulate the progressive loss of strength typically associated with excess pore pressure buildup or structural degradation in cohesive soils. The yield surface remains fixed and does not evolve with accumulated cycles, limiting the model's ability to reproduce cyclic softening or failure mechanisms. These limitations are inherent to the constitutive formulation; more advanced models, such as bounding surface plasticity or effective stress-based formulations, would be required to capture such phenomena.

The PIMY material requires the definition of five parameters to represent the clay behavior under cyclic loading: i) mass density, ii) pressure dependence coefficient, iii) cohesion or undrained shear strength (s_u), iv) rigidity index (G_{max}/s_u), and v) Poisson's ratio (ν). The mass density of the clay was defined as 1.8 Mg/m³. This value corresponds to typical values for Speswhite kaolin clay and is consistent with those reported in previous numerical modeling studies (Soriano et al., 2024). The undrained shear strength (s_u) was defined as a depth-dependent profile as defined in Equation 1. The rigidity index (G_{max}/s_u) controls the shape of the hyperbolic backbone curve and was calibrated to match the experimental load–displacement response. For this model, a value of G_{max}/s_u =350, where G_{max} corresponds to the shear stiffness at small strains, was found to provide the best agreement with the monotonic pile head displacements observed in the centrifuge tests. This ratio reflects the small-strain shear modulus relative to the undrained strength and is used to define the initial tangent stiffness of the soil. The selected value is within the range reported in the literature for soft marine clays: for example, Feng et al. (2019) used G_{max}/s_u =336 in suction caisson analyses, Lai et al. (2021) adopted a range of G_{max}/s_u from 250 to 1000 for monopile models, and Fu et al. (2020a) employed a value of G_{max}/s_u =333 in layered clay profiles.

For the current model, the number of yield surfaces was set to 20 to adequately represent the soil behavior under varying load conditions. In the PIMY soil model, the Von Mises yield surface can be calibrated to fit s_u by adjusting the yield stress in the model to correspond to the undrained strength of the soil. In the current analysis, s_u was assumed to be isotropic. This simplification, although common in numerical modeling, may not capture the anisotropic behavior observed in K_0 consolidated triaxial tests. Table 3 summarizes the parameters employed for the definition of the pile and soil materials.

Table 3. Model calibration parameters

Pile	
E	74 GPa
EI	895 MN•m^2
Mass density, ρ	2.71 Mg/m^3
Clay	
Mass density	1.8 Mg/m^3
Pressure dependence coefficient	0
Cohesion - s_u (without strain rate effects)	1.27+1.17z (kPa)*
Rigidity index G_{max}/s_u	350
Poisson's Ratio - ν	0.49

*Depth z in meters (m)

2.4 Finite Element Mesh

The finite element mesh was designed with a boundary distance from the pile's edge to the mesh's far end set at 20 times the pile diameter (20D), equivalent to approximately 20 meters. Vertically, the extent of the mesh was determined to be twice the pile's embedment length (2L), for a total depth of 32 meters.

At the bottom boundary, all three displacement components were fixed (zero displacement). Additionally, normal displacements were fixed at the vertical boundaries.

The pile was modeled as a volume; to consider the hollow section characteristics of the pile, reduction factors were applied to the gross section to obtain an equivalent area of cross-section and moment of inertia. The numerical model did not account for the effects of pile installation; however, as previously discussed, the model preparation technique for the centrifuge test resembled a "wished-in-place" pile installation.

The undrained shear strength (s_u) profile defined in Equation (1) was discretized into sub-layers with a thickness of 1 m to capture the increase in s_u with depth. This approach is similar to that employed by Soriano et al. (2024) for simulating the behavior of soft clay submarine slope profiles subjected to seismic loading. A scale factor was applied to the undrained shear strength profile presented in Equation 1 to consider strain rate effects as discussed in the following section. For the numerical simulations, no gap was assumed along the pile. This assumption is justified on basis of the analysis by Fu et al. (2020b), who showed that for normally consolidated clays with low undrained shear strength near the seabed, the development of a tension gap behind the pile has a limited impact. This is because the loss of passive resistance at the rear is offset by an increase in the effective earth pressure on the front of the pile. Therefore, for the depth-dependent strength profile considered in this study, the influence of a potential gap is expected to be minimal.

To achieve an acceptable level of mesh refinement while maintaining computational efficiency, a mesh convergence study was performed. The final mesh consisted of 36,080 elements and 37845 nodes for the soil domain and 3,996 elements and 3,997 nodes for the pile. The configuration of this finite element mesh, along with the normalized stress-strain response of the clay (normalized backbone curve), is illustrated in Figure 4.

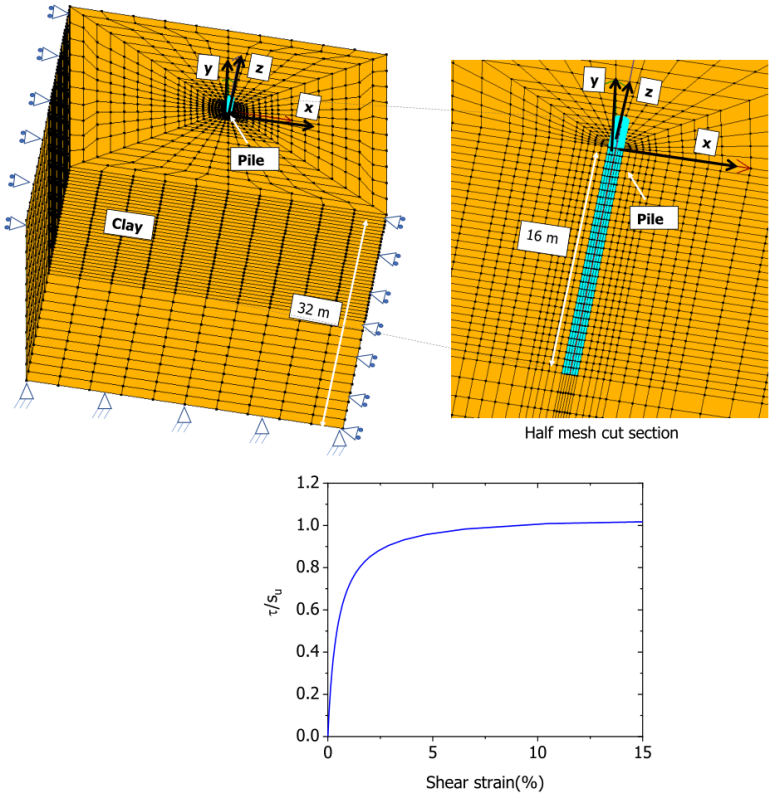

Fig.4. Three-dimensional finite element mesh and backbone curve

3. Numerical Model Calibration

3.1 Monotonic response

The validation of the numerical model was conducted by comparing its monotonic response to that of the centrifuge test SOLCYPC05S1ins, as reported by Khemakhem (2012a). In the centrifuge test, the pile was loaded in a displacement-controlled manner at a rate of 20 mm/s (prototype scale). This means that a displacement of 100 mm (or approximately 0.1D) was reached in about 5 seconds, which is significantly faster than standard monotonic DSS tests and has implications for strain rate effects (Andersen, 2015). An initial model was run using the undrained shear strength profile from Equation (1), which resulted in an overprediction of the pile head displacement, as depicted in Figure 5.

On the basis of the back-analyses conducted by Zhang et al. (2020), the s_u profile was increased by 25% to account for these rate effects. The adjusted model demonstrated an improved match when compared with the experimental pile head displacements. With the model now considering strain rate effects, additional comparisons were conducted in terms of bending moments observed at two distinct levels of pile loading, as shown in Figure 5. The analyses were conducted at the prototype scale, using the geometric parameters provided in Table 1. From this point forward, the analyses and results presented in this paper consider the adjusted undrained shear strength profile.

The monotonic test revealed an ultimate load (H_{ult}) of approximately 350 kN. Furthermore, by applying a safety factor of 1.5, a serviceability state load (H_{SLS}) of 233 kN was obtained, corresponding to a normalized displacement of approximately 11% of the pile diameter ($\Delta h/B$).

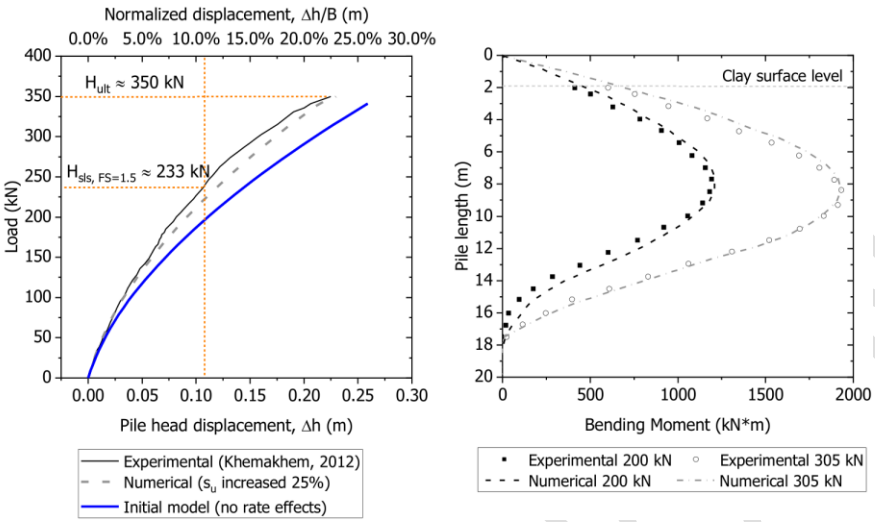

Fig.5. Comparison of monotonic load response: experimental data versus numerical model results for pile head displacement and bending moments

3.2 Cyclic response

To evaluate the cyclic response of the numerical model, two centrifuge tests from Khemakhem (2012a) were selected: test C09S1ins and test C01S1ins. In both experiments, the load was applied at the pile head. The load was maintained at an average level of H_{avg}=150 kN, while the cyclic component was varied. During the centrifuge experiment, an initial load was applied at a rate of 50 kN/s until the average load level (H_{avg}) was reached, followed by the cyclic load amplitude (H_{cyc}). The load cycles were subsequently applied at a rate of 0.25 Hz. Figure 6 illustrates the cyclic load definitions employed in the centrifuge tests and numerical models. Specifically, for the test identified as C09S1ins, 40 load cycles were applied with a cyclic amplitude of H_{cyc}=200 kN, resulting in load reversals applied to the pile. For test C02S1ins, 1000 cycles were applied with a cyclic amplitude of 50 kN.

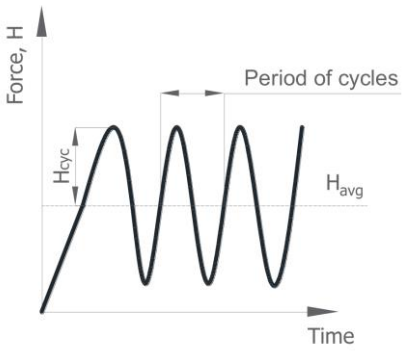

Model	Number of cycles	H_{avg} (kN)	H_{cyc}(kN)
C09S1ins	40	150	200
C01S1ins	100	150	50

Fig.6. Cyclic load definitions

Figure 7 and Figure 8 present the outcomes of the cyclic load models, focusing on the comparison of accumulated pile displacements versus the number of cycles and the bending moment profiles at a given number of cycles. The results are also compared with those of the back-analyses conducted by Zhang et al. (2020).

The results show that for the large-amplitude cyclic load test (C09S1ins in Figure 7), the numerical model follows the accumulation of pile head displacements up to approximately 20 load cycles (N=20). This trend aligns with the numerical model of Zhang et al. (2020), which exhibits a similar response. However, Khemakhem (2012a) reported an abrupt increase in the rate of cyclic displacement accumulation beyond 20 cycles in the C09S1ins experiment, suggesting large soil plastification. This divergence is attributed to the PIMY model's formulation. As a total stress-based model, it does not explicitly calculate the accumulation of pore water pressure. Instead, the effects of phenomena such as pore pressure build-up and clay destructuration are implicitly included by calibrating the model against the accumulated displacements from the cyclic tests. The abrupt increase in the experimental displacement rate after 20 cycles is likely due to significant pore pressure accumulation, leading to a reduction in cyclic the stiffness and strength, an effect that the current model does not capture.

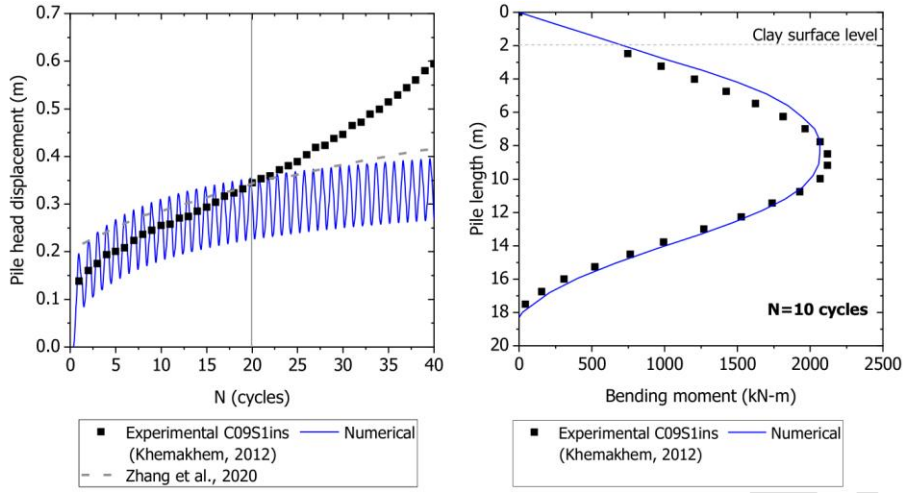

Fig. 7. Cyclic load model response compared with experimental data for test C09S1ins (Hcyc=200 kN)

For the low-amplitude model (C01S1ins in Figure 8), the numerical model closely follows the trend observed in the reference test, even at relatively large numbers of load cycles. However, it slightly underestimates the accumulated displacements. Moreover, the back-analysis curve of Zhang et al. (2020) underpredicted the experimental data. In terms of bending moments, for the load cycles selected for comparison, the numerical model was able to follow the test measurements for the low and large amplitude loading conditions.

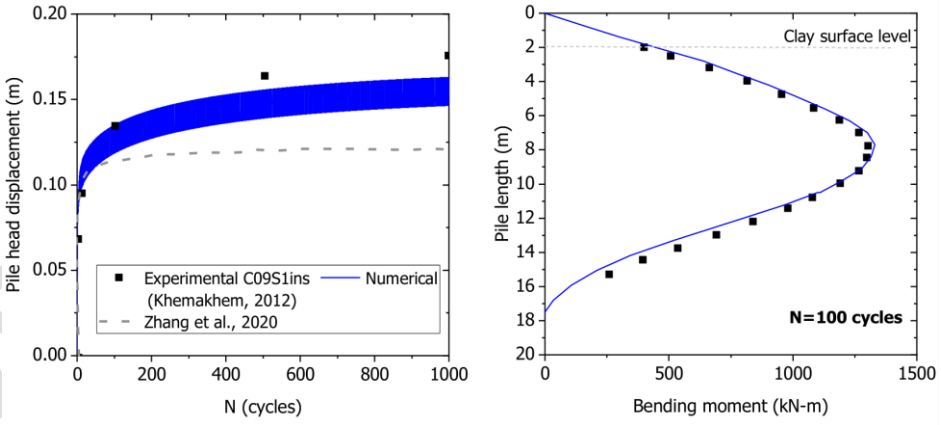

Fig. 8. Cyclic load model response compared with experimental data for test C01S1ins (Hcyc=50 kN)

4. Parametric study

To evaluate the performance of the numerical model under various loading conditions, a parametric study was conducted. The baseline for this study was established using the soil profile and pile geometry from the model calibration. The study involved applying cyclic loads in different scenarios:

- Unidirectional cyclic loading with variations in both average and cyclic load amplitudes.

- Multidirectional loading.

The primary objective was to assess how the model responds to various combinations of average and cyclic loads. This also served to evaluate the capabilities of the modelling approach proposed in this research. For the peak load in the models, a safety factor (FS) of 1.5 was applied to the ultimate load (H_{ult} = 350 kN) obtained from the monotonic model to simulate an operational load condition.

For the estimation of multidirectional loads on the anchor pile, a purely horizontal load condition was assumed. This simplification is representative of a catenary mooring line configuration, where the inherent weight of the line ensures that a segment rests on the seabed, resulting in a load that is effectively horizontal at the anchor padeye. This assumption is consistent with recent studies on shared anchor systems for floating offshore wind turbines (Fontana et al., 2018; Lovera et al., 2025; Zabatta et al., 2025). A summary of the load scenarios used in the numerical simulations is provided in Table 4.

Table 4. List of numerical models for parametric analyses

Model	H_{ult} (kN)	FS	H_{max} (kN)	H_{avg} (kN)	H_{cyc}(kN)	N(cycles)
M1	350	1.5	233.3	116.7	116.7	100
M2	350	1.5	233.3	175.0	58.3	100
M3	350	1.5	233.3	58.3	175.0	100
M4	350	1.5	233.3	0.0	233.0	100
M5	Variable amplitude load - increasing amplitude					1228
M6	Variable amplitude load - decreasing amplitude					1228
DLC 1.6 WWC 0°	Multidirectional load - three mooring lines					
DLC 1.6 WWC 30°	Multidirectional load - three mooring lines					
DLC 1.6 WWC 60°	Multidirectional load - three mooring lines					

Figure 9 presents an interaction diagram summarizing the load configurations of models M1 to M4. This diagram utilizes normalized values for the average load component (H_{avg}/H_{ult}) and the cyclic load component (H_{cyc}/H_{ult}), where H_{ult} is the ultimate load. The load cases from the validation models C09S1ins and C01S1ins are also included for comparison.

The interaction diagram reveals that the large load amplitude scenario from test C09S1ins falls within the boundary that delimits unstable behavior under cyclic loading. This aligns with the observed experimental response in Figure 7, where a significant increase in cyclic displacements occurs after 20 cycles.

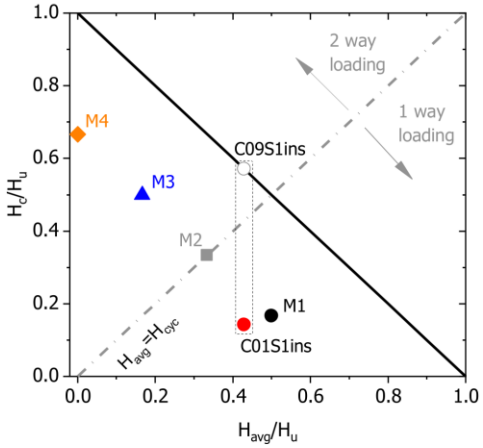

Fig. 9. Interaction diagram for the pile model showing unidirectional load cases M1-M4 and validation tests

Figure 10 illustrates the load compositions applied to model M5 and model M6 along with a representation of the trajectories followed within the interaction diagram. These compositions (number of cycles at different constant cyclic load amplitudes) were based on the conceptual transformation of a design storm into load parcels presented by Andersen (2015).

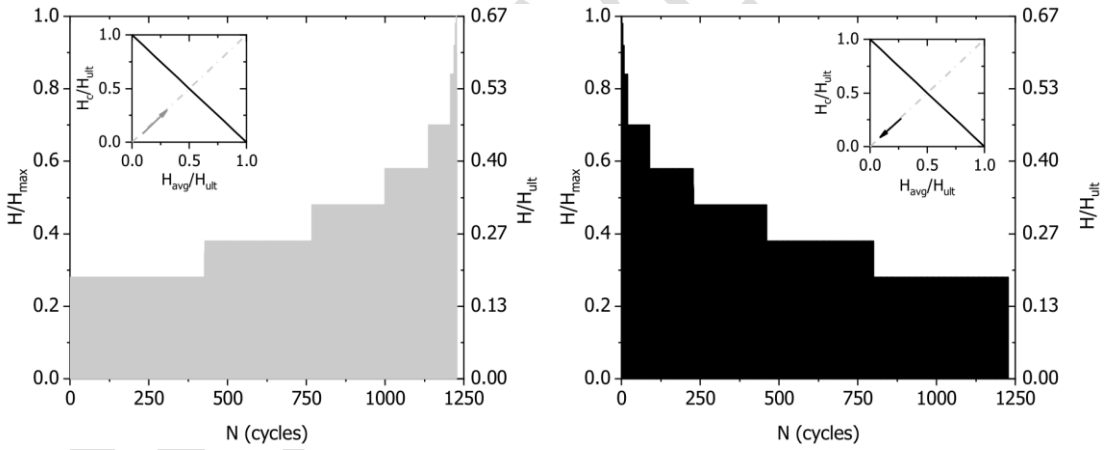

Fig. 10. Variable-amplitude load sequence based on the load parcel concept (Andersen, 2015)

5. Results

5.1 Effects of Cyclic and Average Load

Figure 11 shows the displacement histories in relation to the number of cycles applied to models M1 to M4. These models were subjected to the same peak load, with varying combinations of average and cyclic loads. Model M2, which had a high average load (Havg = 175 kN) and a low cyclic amplitude (Hcyc = 58.3 kN), resulted in the greatest accumulation of permanent displacements. This reflects the influence of the sustained average load in driving long-term pile head displacements, even when the cyclic component is smaller. In contrast, model M1, with equal average and cyclic loads (Havg = Hcyc = 116.7 kN), showed smaller permanent displacements than M2 but larger cyclic amplitudes due to the

greater load variation. Model M3, dominated by the cyclic component (Hcyc = 175 kN), exhibited larger displacement amplitudes but less permanent accumulation compared to M2. Models M3 and M4 introduced load reversals, with model M4 having the largest reversal. These reversals appear to stabilize the response and reduce the net accumulation of displacements over cycles.

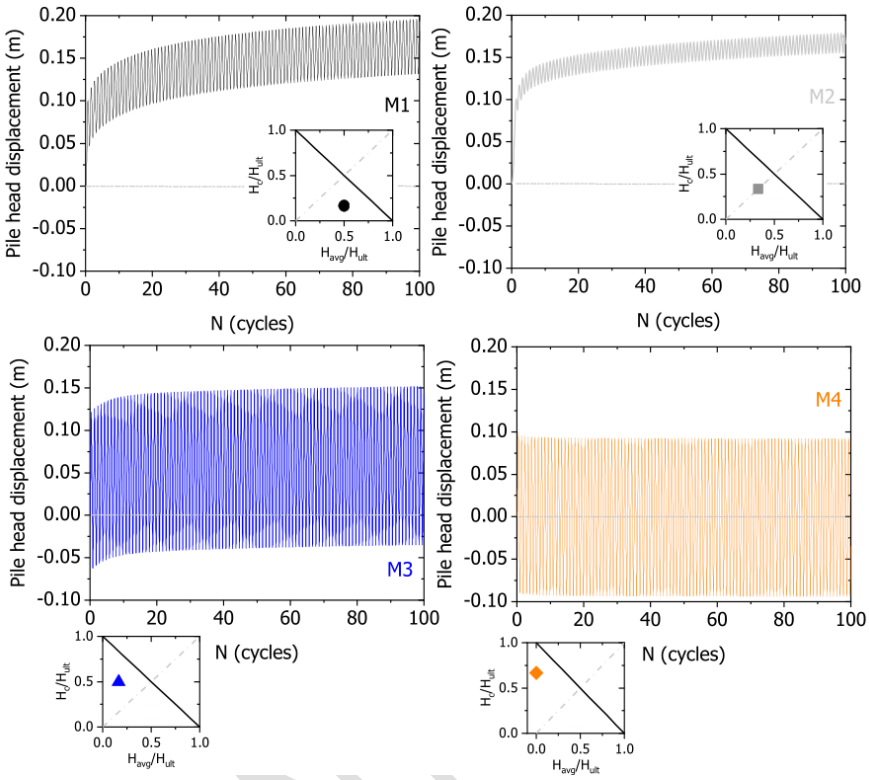

Fig. 11. Pile head displacements with increasing number of load cycles: models M1 to M4

To examine the accumulation of displacements, the peak displacement for each cycle (DN) was normalized by the peak displacement at the first loading cycle (D_1). Figure 12 provides a summary of the normalized displacements (D_N/D_1) as the number of loading cycles increases. The normalized displacements were fitted using a logarithmic function (Lin and Liao, 1999):

$$\frac{D_N}{D_1} = 1 + \alpha \ln(N) \tag{4}$$

where α is an attenuation parameter related with the pile head displacement as the number of cycles (N) increases. The curves shown in Figure 12 include the calculation of the root mean square error (RMSE) ranging from values of normalized displacement of 0.014 to 0.020. The results indicate that the normalized displacements exhibit the highest values when the average and cyclic loads are equal (model M1). Model M2 presents a similar trend to that of model M1, with slightly lower values of normalized displacement accumulation. Finally, the models incorporating load reversals (M3 and M4) display a stabilization of the normalized displacements as the number of cycles increases. Although the

numerical simulations here refer to piles subjected to lateral cyclic loading, the load reversal condition can be associated with multiline anchors (Fontana et al., 2018), and the results provide insights into the stabilizing effects on displacement accumulation when load reversals occur in piles installed in soft clay.

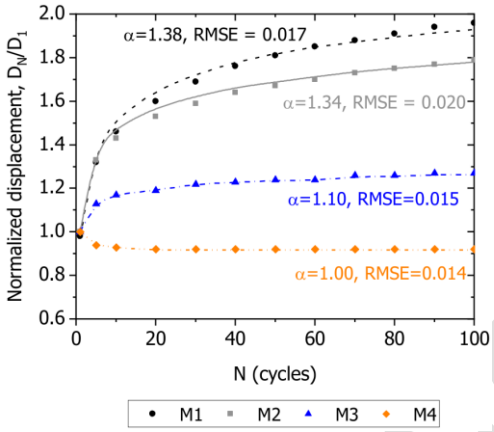

Fig. 12. Normalized displacements versus number of cycles for models M1 to M4, with logarithmic curve fits.

5.2 Varying Amplitude Loads

Figure 13 shows the load-displacement curves obtained from the application of the variable amplitude load sequences depicted in Figure 10. The objective was to evaluate the model's performance under a high number of cycles (>1000 cycles) using a well-established load history employed in offshore foundation applications. The results exhibit a distinct response depending on the order of the application of the loading packages.

In the case of the decreasing load amplitude sequence (model M6), there is an initial generation of large peak and permanent displacements. This is subsequently followed by a decrease in both peak and permanent components. Upon the completion of 1250 cycles, the increasing amplitude load sequence (model M5) resulted in larger permanent displacements of around 11 cm. This contrasts with the reducing amplitude load sequence, which yielded permanent displacements of approximately 7 cm (model M6). This difference can be attributed to the cumulative damage caused by the larger load amplitudes applied later in the loading sequence for Model M5, leading to more pronounced plastic deformation in the soil surrounding the pile. Similar behavior has been observed in numerical models of caissons in clay subjected to cyclic loading under total stress assumptions (Al-Ramthan and Aubeny, 2020; Al-Janabi and Aubeny, 2022). It is worth noting, however, that effective stress-based models may capture a different response, where early high-amplitude loading generates excess pore pressures and stress redistribution, potentially leading to greater displacement accumulation under subsequent smaller cycles.

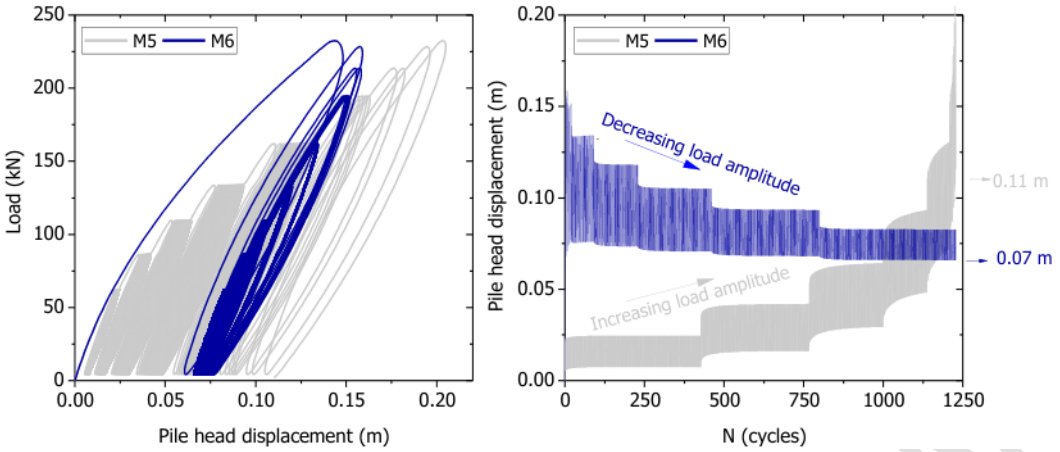

409

410 **Fig. 13.** Variable amplitude load response: increasing load packages (M5) and decreasing loading
411 packages (M6)

412 ## 5.3 Multidirectional Load

413 To replicate the complex loading conditions experienced by offshore anchoring systems, a
414 multidirectional load configuration was incorporated into the model. This configuration simulates the
415 convergence of three mooring lines at the pile head, replicating the multiline anchor concept increasingly
416 employed in floating wind farm deployments such as Hywind Tampen, WindFloat and Hybrid Spar
417 (Fontana et al., 2018). Figure 14 illustrates a schematic comparison of single and multiline anchor
418 geometries.

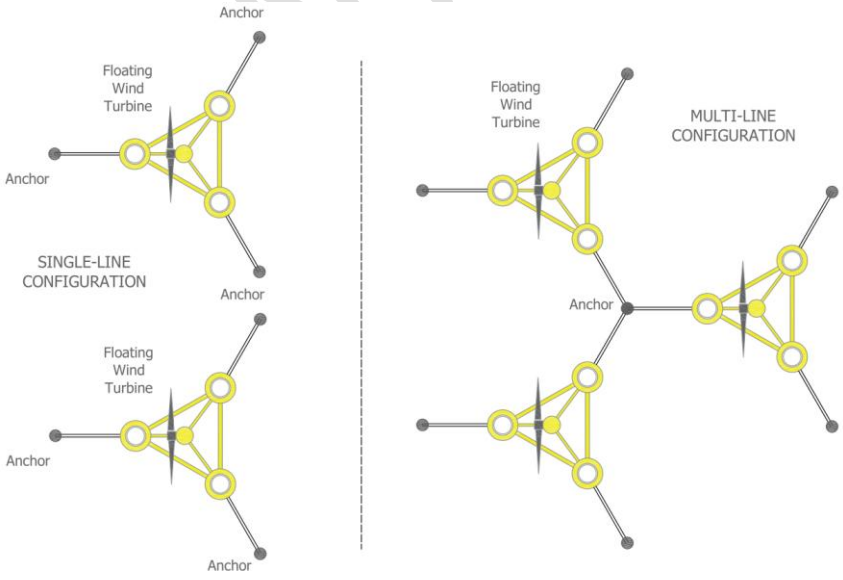

419

420 **Fig. 14.** Representation of single line and multiline anchor configurations for floating wind turbines

421 The load set for the multiline anchor configuration was derived from the calculations presented by
422 Balakrishnan et al., (2020) for a multiline anchor configuration employing the NREL 5 MW with OC3
423 spar-buoy supported turbines (Jonkman, 2010). Figure 15 depicts an idealized configuration with three

mooring lines converging at a single pile, with 120-degree angular separation between each line. The tension forces for each wind turbine are denoted as $\overrightarrow{H_1}$, $\overrightarrow{H_2}$, and $\overrightarrow{H_3}$, while $\overrightarrow{H_{multi}}$ represents the resultant force, or combined force acting on the pile due to the shared anchor system. The individual mooring line tensions were converted into the resultant force $\overrightarrow{H_{multi}}$ using vector summation.

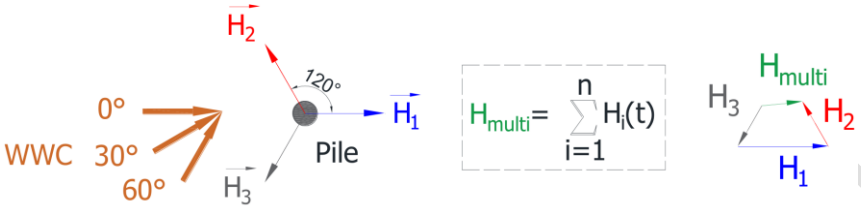

Fig. 15. Forces acting in a three mooring line configuration

Three load cases (DLC 1.6 WWC 0°, DLC WWC 30°, and DLC WWC 60°) were selected to represent varying wind, wave, and current (WWC) orientations ranging from 0° to 60°. These load sets were adapted from the work of Balakrishnan et al. (2020) to be compatible with the current numerical model through a two-step normalization and scaling procedure.

First, normalization was performed independently for each load case, using the peak forces of relevant load components (H1 for DLC 1.6 WWC 0° and DLC WWC 30°, and H2 for DLC WWC 60°) as normalization factors. This process yields dimensionless load multipliers ranging from 0 to 1, a common approach in nonlinear finite element analyses that allows for the preservation of realistic load patterns while enabling flexible scaling for various structural capacities (Smith, 2009). The normalized multipliers thus maintain the relative contributions of the wind, wave, and current effects on each mooring line.

Second, the load multipliers were scaled by a reference peak load (H_{max}) of 233 kN for each relevant load component. This reference load was determined from the maximum pile load recorded during centrifuge testing (Hult = 350 kN), which was reduced by a safety factor of 1.5. This scaling method aligns with strategies applied in similar numerical studies (Al-Ramthan et al., 2020) and corresponds to a load that produces a pile head displacement of approximately 10% of the pile diameter—a common serviceability limit state (CFMS, 2020).

This combined normalization and scaling procedure ensures that the applied loads remain within realistic bounds while preserving the relative load contributions and temporal characteristics of the original dataset. Figure 16 illustrates the distribution of scaled load multipliers on the pile head in both horizontal (x) and transverse (y) directions for the DLC 1.6 WWC 0° load case.

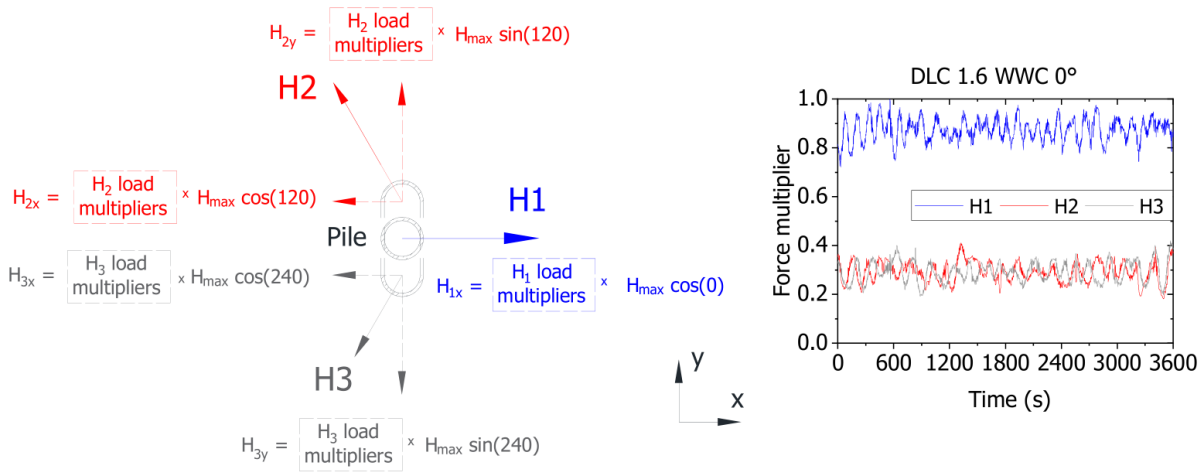

451

452 **Fig. 16.** Representation of the application of load multipliers to the model

453 The scaled time histories and polar plot representations of the multidirectional forces (H_{multi}) applied to
454 the numerical model are presented in Figure 17, Figure 18, and Figure 19. For the DLC 1.6 WWC 0°
455 and DLC 1.6 WWC30° load cases, the resultant forces closely follow the WWC directions, indicating a
456 dominant influence from these aligned components. In contrast, the DLC 1.6 WWC 60° case exhibits a
457 resultant force aligning more closely with the orientation of the predominant load component, H_2, at an
458 average angle of 120 degrees. This behavior can be attributed to the shift in the peak loads toward H_2,
459 combined with the relatively similar magnitudes of H_1 and H_3.

460

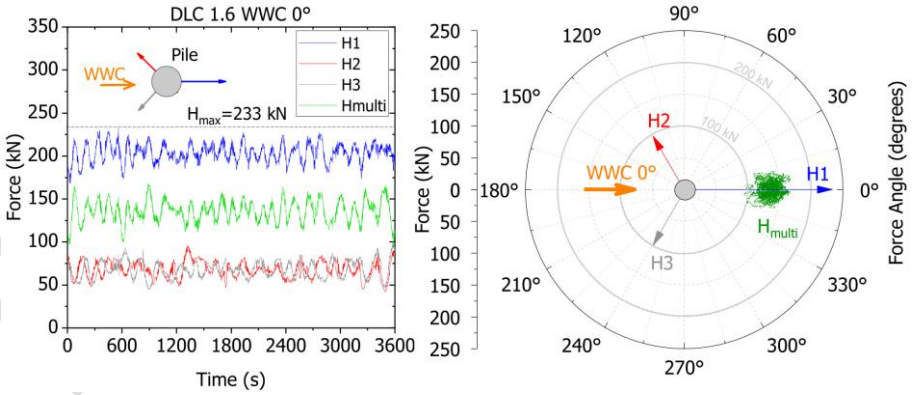

461

462 **Fig. 17.** Scaled time histories of forces applied to the pile model, with a WWC of 0°

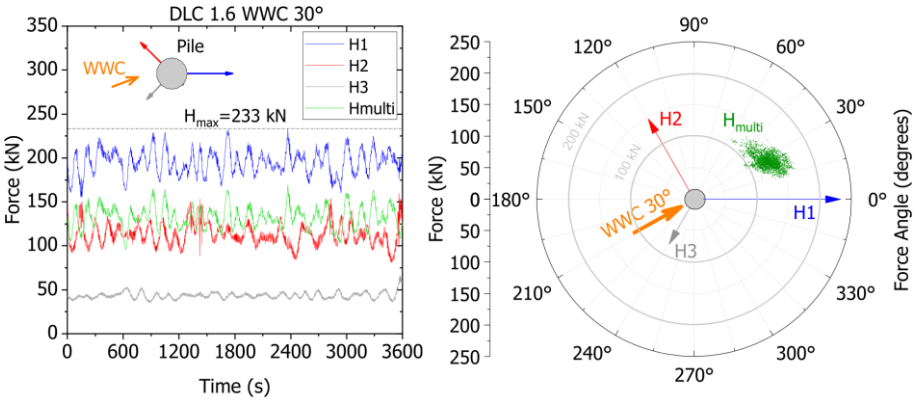

Fig. 18. Scaled time histories of forces applied to the pile model, with a WWC of 30°

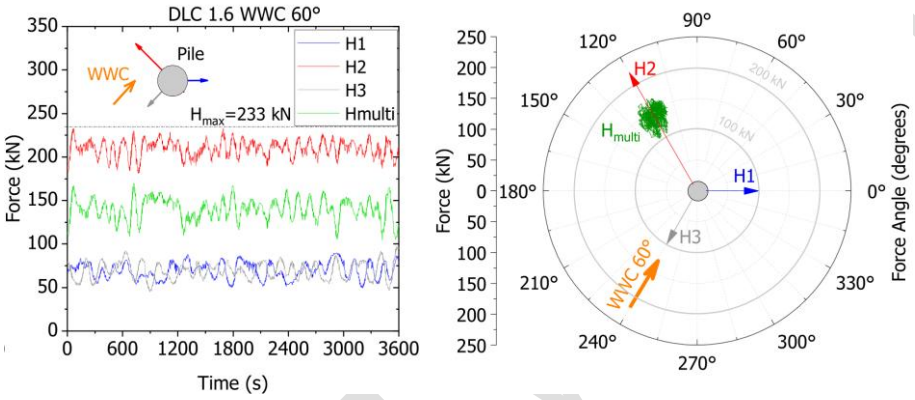

Fig. 19. Scaled time histories of forces applied to the pile model, with a WWC of 60°

Figure 20 summarizes the pile head displacements observed in the numerical model for the different load cases. As expected, the displacements increase from zero due to the application of the average load component acting in the direction of the resultant force (H_{multi}). Table 5 shows that for load cases DLC 1.6 WWC 0° and DLC 1.6 WWC 30°, the mean angle of the resultant displacements aligns with the WWC directions. For the DLC 1.6 WWC 60° load case, the observed shift in resultant displacements corresponds to the previously discussed dominance of the H_2 load component.

Once the average load value is reached, the displacement accumulation patterns are influenced by the specific components of the multidirectional load. Notably, Table 5 reveals similar resultant and peak displacement magnitudes across all three cases. This behavior supports the suitability of axisymmetric anchors, such as piles or suction caissons, for shared anchor systems.

Table 5. Summary of multidirectional displacements

	Resultant displacements		Angle		
Load Case	Mean (m)	Max(m)	Min (deg)	Mean (deg)	Max(deg)
DLC 1.6 WWC 0°	0.08	0.09	-6	0	6
DLC 1.6 WWC 30°	0.08	0.1	21	28	44
DLC 1.6 WWC 60°	0.08	0.09	113	120	124

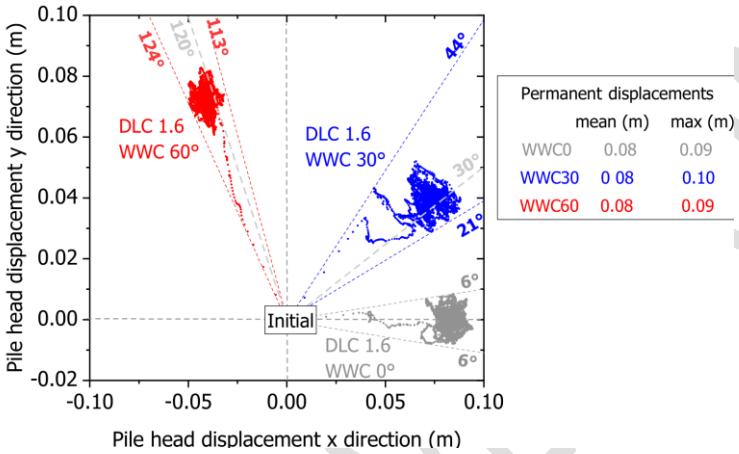

Fig. 20. Multidirectional displacements for load cases DLC 1.6 WWC0°, DLC 1.6 WWC30°and DLC 1.6 WWC60°

6. Discussion

While the numerical model shows good agreement with centrifuge test data for monotonic and unidirectional cyclic loading, its application to multidirectional scenarios (e.g., DLC 1.6 WWC 0°/30°/60°) lacks direct validation against physical test data for piles in clay. This is largely due to the limited experimental data in the literature concerning the performance of piles in cohesive soils under such complex loading. Recent relevant research includes observations from tests on shared anchor piles in sand subjected to multidirectional loading (Abadie, 2025). Furthermore, the development of new experimental capabilities, such as a setup for testing multidirectional loads on suction anchors in normally consolidated kaolin clay has been reported by Soriano et al. (2025).

In the current study, multidirectional effects are indirectly captured through the superposition of load vectors and the inherent plastic response of the soil model. However, the constitutive model does not include specific features to represent directional soil fabric or anisotropic degradation, and its limitations in this context are recognized. Therefore, the numerical predictions presented here should be interpreted as a foundational step toward modeling shared anchors under multidirectional loading. Future validation work is planned to support and refine this approach as new experimental data become available.

7. Conclusions

The numerical model developed in this study provides valuable insights into the cyclic response of offshore piles in soft clay. The model captured the primary trends of displacement accumulation observed in the centrifuge tests, showing good agreement with the experimental response for initial loading cycles and low-amplitude scenarios. While the proposed approach is a valuable tool for assessing pile performance, its limitations, such as not capturing the abrupt increase in the rate of displacement accumulation observed experimentally after a higher number of cycles, are acknowledged.

A primary contribution of this research is the development and application of a methodology to analyze pile anchors under the complex, multidirectional loading characteristic of shared anchor systems. Faced with a scarcity of established procedures and publicly available load datasets, this study introduces a practical workflow for scaling and applying such loads.

The parametric study highlighted the influence of various cyclic load combinations on the pile response. The scenarios with a high sustained average load component (models M1 and M2) are the primary drivers of permanent displacement accumulation. In contrast, the introduction of load reversals (Models M3 and M4) was shown to counteract this one-directional accumulation, resulting in reduced net permanent displacements over the applied cyclic loading histories.

The investigation of different wind, wave, and current (WWC) orientations (0°, 30°, and 60°) highlighted the influence of load component dominance on the resultant forces. A key finding was that the resultant and peak displacements remained similar across all tested WWC orientations. This consistent performance, irrespective of the primary load direction, supports the suitability of an axisymmetric pile configuration for complex applications such as shared anchor systems, where load directionality can vary significantly.

This study adopted a simplified assumption of homogeneous soil properties; however, natural clay deposits and even reconstituted centrifuge models may exhibit spatial variability. Such variability, characterized by vertical and horizontal correlation lengths (Phoon and Kulhawy, 1999), may influence the development of displacements, bending moments, and failure mechanisms. Although the use of uniform soil parameters facilitates the interpretation of the model response and improves computational efficiency, future studies should incorporate spatial variability to assess its influence on local and global pile behavior under multidirectional cyclic loading.

Finally, the study has certain limitations stemming from the chosen constitutive model. The 'PressureIndependentMultiYield' (PIMY) model is a total-stress formulation and does not explicitly account for history-dependent phenomena such as pore pressure accumulation or the associated degradation of soil strength and stiffness. While the model implicitly captures permanent strain accumulation through kinematic hardening, this behavior is an emergent property rather than a directly

controlled parameter. Further validation with field data from instrumented piles under real-world loading conditions would strengthen the model's generalizability.

Acknowledgements

This research has received funding from the European Union's Horizon 2020 research and innovation programme under the Marie Skłodowska-Curie grant agreement: 101106921 - Project ShareWind.

References

Abadie, C. N. (2025). Shared anchor pile response to multidirectional lateral cyclic loading. In Proceedings of the 5th International Symposium on Frontiers in Offshore Geotechnics (ISFOG2025) (Bright Spark Lectures). https://doi.org/10.53243/ISFOG2025-654

Al-Janabi, H.A., Aubeny, C.P., 2022. Experimental and numerical investigation of the performance of piles and suction caissons subjected to inclined cyclic loading in cohesive soils. *Journal of Geotechnical and Geoenvironmental Engineering* 148, 04022036. doi:10.1061/(ASCE)GT.1943-5606.0002789.

Al-Ramthan, A.Q.O., Aubeny, C.P., 2020. Numerical investigation of the performance of caissons in cohesive soils under cyclic loading. *International Journal of Geomechanics* 20, 04020042. doi:10.1061/(ASCE)GM.1943-5622.0001650.

Andersen, K., 2015. Cyclic soil parameters for offshore foundation design. *Frontiers in Offshore Geotechnics III* 5, 5–82.

Aubeny, C., 2017. *Geomechanics of Marine Anchors*. CRC Press. doi:10.4324/9781351237376.

Balakrishnan, K., Arwade, S.R., DeGroot, D.J., Fontana, C., Landon, M., Aubeny, C.P., 2020. Comparison of multiline anchors for offshore wind turbines with spar and with semisubmersible. *Journal of Physics: Conference Series* 1452, 012032. doi:10.1088/1742-6596/1452/1/012032.

Brussa, G., Grosso, M., Rigamonti, L., 2023. Life cycle assessment of a floating offshore wind farm in Italy. *Sustainable Production and Consumption* 39, 134–144. doi:https://doi.org/10.1016/j.spc.2023.05.006.

Burns, M., Landon Maynoard, M., Davids, W., Chung, J., Gaudin, C., 2014. Centrifuge modelling of suction caissons under orthogonal double line loading, in: *Physical Modelling in Geotechnics: Proceedings of the 8th International Conference on Physical Modelling in Geotechnics 2014 (ICPMG2014)*, CRC Press. pp. 654–471. doi:10.1201/b16200-63.

Cerfontaine, B., Knappett, J.A., Brown, M.J., Bradshaw, A.S., 2019. Effect of soil deformability on the failure mechanism of shallow plate or screw anchors in sand. *Computers and Geotechnics* 109, 34–45. doi:https://doi.org/10.1016/j.compgeo.2019.01.007.

Cerfontaine, B., White, D., Kwa, K., Gourvenec, S., Knappett, J., Brown, M., 2023. Anchor geotechnics for floating offshore wind: Current technologies and future innovations. *Ocean Engineering* 279, 114327. doi:https://doi.org/10.1016/j.oceaneng.2023.114327.

CFMS, 2020. Recommendations for planning and designing foundations of offshore wind turbines. French Society on Soil Mechanics and Geotechnical Engineering. https://hal.archives-ouvertes.fr/hal-03808550

Chung, J., 2012. Physical Modeling of Suction Caissons Loaded in Two Orthogonal Directions for Efficient Mooring of Offshore Wind Platforms. Master's thesis. University of Maine. URL: https://digitalcommons.library.umaine.edu/etd/1754.

Edwards, E.C., Holcombe, A., Brown, S., Ransley, E., Hann, M., Greaves, D., 2023. Evolution of floating offshore wind platforms: A review of at-sea devices. *Renewable and Sustainable Energy Reviews* 183, 113416. doi:https://doi.org/10.1016/j.rser.2023.113416.

Feng, X., Gourvenec, S., White, D.J., 2019. Load capacity of caisson anchors exposed to seabed trenching. *Ocean Engineering* 171, 181–192. doi:https://doi.org/10.1016/j.oceaneng.2018.09.027.

Fontana, C.M., Hallowell, S.T., Arwade, S.R., DeGroot, D.J., Landon, M.E., Aubeny, C.P., Diaz, B., Myers, A.T., Ozmutlu, S., 2018. Multiline anchor force dynamics in floating offshore wind turbines. *Wind Energy* 21, 1177–1190. doi:https://doi.org/10.1002/we.2222.

Fu, D., Zhang, Y., Aamodt, K.K., Yan, Y., 2020a. A multi-spring model for monopile analysis in soft clays. *Marine Structures* 72, 102768. doi:https://doi.org/10.1016/j.marstruc.2020.102768.

Fu, D., Zhang, Y., Yan, Y., Jostad, H. P. (2020b). Effects of tension gap on the holding capacity of suction anchors. *Marine Structures, 69*, 102679. https://doi.org/10.1016/j.marstruc.2019.102679

Garnier, J., Gaudin, C., Springman, S., Culligan, P., Goodings, D., Konig, D., Kutter, B., Phillips, R., Randolph, M., Thorel, L., 2007. Catalogue of scaling laws and similitude questions in geotechnical centrifuge modelling. *International Journal of Physical Modelling in Geotechnics* 7, 01–23. doi:10.1680/ijpmg.2007.070301.

Gogoi, R., Aldawwas, A., Aubeny, C., Martinez, A., Huang, L., DeGroot, D.J., Arwade, S., Beemer, R.D., 2023. Numerical analyses of a multiline ring anchor for floating offshore wind turbines in sand, in: *Proceedings of the 10th European Conference on Numerical Methods in Geotechnical Engineering (NUMGE2023)*. doi:10.53243/NUMGE2023-336.

Hallowell, S.T., Arwade, S.R., Fontana, C.M., DeGroot, D.J., Aubeny, C.P., Diaz, B.D., Myers, A.T., Landon, M.E., 2018. System reliability of floating offshore wind farms with multiline anchors. *Ocean Engineering* 160, 94–104. doi:https://doi.org/10.1016/j.oceaneng.2018.04.046.

Herduin, M., 2019. Multi-directional loading on shared anchors for offshore renewable energy: Definition and preliminary investigation into soil behaviour and anchor performance. Ph.D. thesis. The University of Western Australia. doi:10.26182/5d2fd93d88ce7.

Jonkman, J., 2010. Definition of the floating system for phase iv of oc3. NREL Technical Report NREL/TP-500-47535 (United States: National Renewable Laboratory Golden Colorado) URL: https://www.osti.gov/biblio/979456, doi:10.2172/979456.

Khemakhem, M., 2012a. Etude experimentale de la réponse aux charges latérales monotones et cycliques d'un pieu fore dans l'argile. Ph.D. thesis. Ecole centrale de Nantes 2012. URL: http://www.theses.fr/2012ECDN0026.

Khemakhem, M., Chenaf, N., Garnier, J., Favraud, C., Gaudicheau, P., 2012b. Development of Degradation Laws For Describing the Cyclic Lateral Response of Piles In Clay. Offshore Site Investigation and Geotechnics: Integrated Technologies - Present and Future, London, United Kingdom, SUT–OSIG–12–27.

Khemakhem, M., Chenaf, N., Garnier, J., Rault, G., Thorel, L., Dano, C., 2010. Laterally static and cyclic pile behavior in clay, in: *7th International Conference on Physical Modelling in Geotechnics*, Zurich, Switzerland. URL: https://hal.science/hal-01008379.

Kondner, R.L., 1963. Hyperbolic stress-strain response: cohesive soils. *Journal of the Soil Mechanics and Foundations Division* 89, 115–143. doi:10.1061/JSFEAQ.0000479.

Lau, B.H. 2015. Cyclic behaviour of monopile foundations for offshore wind turbines in clay. Ph.D. dissertation, University of Cambridge, UK

Kwa, K., Festa, O.G., White, D., Sobey, A., Gourvenec, S., 2023. Integrated numerical modelling of soil-anchor-mooring line-floater response for floating offshore wind, in: Zdravkovic, L., Kontoe, S., Tsiampousi, K., Taborda, D. (Eds.), *Proceedings 10th NUMGE: 10th European Conference*

on Numerical Methods in Geotechnical Engineering, International Society for Soil Mechanics and Geotechnical Engineering.

Lai, Y., Wang, L., Zhang, Y., Hong, Y., 2021. Site-specific soil reaction model for monopiles in soft clay based on laboratory element stress-strain curves. *Ocean Engineering* 220, 108437. doi:https://doi.org/10.1016/j.oceaneng.2020.108437.

Lee, J., Zhao, F., Dutton, A., Backwell, B., Qiao, L., Liang, W., Clarke, E., 2020. Global offshore wind report 2021. *Global Wind Energy Council* 5.

Lin, S.S., Liao, J.C., 1999. Permanent strains of piles in sand due to cyclic lateral loads. *Journal of Geotechnical and Geoenvironmental Engineering* 125, 798–802. doi:10.1061/(ASCE)1090-0241(1999)125:9(798).

Lovera, A., Coquio, T., Peyrard, C. (2025). Analysis of loads applied on floating wind turbines shared anchors. Ocean Engineering, 324(1), 120627. https://doi.org/10.1016/j.oceaneng.2025.120627

McKenna, F., Fenves, G.L., Scott, M.H., 2000. Open system for earthquake engineering simulation. Technical Report.

Mroz, Z. (1967). On the description of anisotropic work hardening. Journal of the Mechanics and Physics of Solids, 15(3), 163–175. https://doi.org/10.1016/0022-5096(67)90030-0

Phoon, K. K., Kulhawy, F. H. (1999). Evaluation of geotechnical property variability. *Canadian Geotechnical Journal*, 36(4), 625–639. https://doi.org/10.1139/t99-039

Poulos, H.G., Hull, T.S., 1989. The role of analytical geomechanics in foundation engineering, in: *Foundation engineering: Current principles and practices*, ASCE. pp. 1578–1606.

Prevost, J., 1985. A simple plasticity theory for frictional cohesionless soils. *International Journal of Soil Dynamics and Earthquake Engineering* 4, 9–17. doi:https://doi.org/10.1016/0261-7277(85)90030-0.

Puech, A., Garnier, J., 2017. *Design of Piles Under Cyclic Loading: SOLCYP Recommendations*. Civil engineering and geomechanics series, ISTE, Limited. doi:10.1002/9781119469018.

Rezaei, F., Contestabile, P., Vicinanza, D., Azzellino, A., 2023. Towards understanding environmental and cumulative impacts of floating wind farms: Lessons learned from the fixed-bottom offshore wind farms. *Ocean Coastal Management* 243, 106772. URL:

https://www.sciencedirect.com/science/article/pii/S0964569123002971, doi:https://doi.org/10.1016/j.ocecoaman.2023.106772.

Smith, M. (2009). ABAQUS/Standard User's Manual, Version 6.9. Dassault Systèmes Simulia Corp.

Soriano, C., Almeida, M.C.F., Almeida, M.S.S., Madabhushi, G., Carlton, B., 2024. Numerical modelling of the seismic response of gentle slopes in southeastern Brazil. *Marine Georesources and Geotechnology* 42, 127–140. doi:10.1080/1064119X.2022.2152511.

Soriano, C., Thorel, L., Blanc, M., Audrain, P. (2025). Centrifuge modelling of cyclic loading on suction anchors in soft clay. In 5th International Symposium on Frontiers in Offshore Geotechnics (ISFOG2025). Theme 11 - Suction installed foundations and anchors). https://doi.org/10.53243/ISFOG2025-424

Spicer, C.A., Abadie, C.N., Madabhushi, G., 2022. Anchor Pile Design for Floating Offshore Wind Turbines, in: *3rd International Conference on Natural Hazards and Infrastructure (ICONHIC)*, Apollo - University of Cambridge Repository, Athens, Greece. URL: https://hal.science/hal-04312226, doi:10.17863/CAM.91865.

Yan, B., Zhu, W., Gao, B., Ye, G., Tian, Y., Wang, Y., 2024. Bearing capacity analysis and mechanism study of shared caisson under multidirectional loading. *Ocean Engineering* 301, 117530. doi:https://doi.org/10.1016/j.oceaneng.2024.117530.

Yang, Z., Elgamal, A., Parra, E., 2003. Computational model for cyclic mobility and associated shear deformation. *Journal of Geotechnical and Geoenvironmental Engineering* 129, 1119–1127. doi:10.1061/(ASCE)1090-0241(2003)129:12(1119).

Zabatta, R., Abadie, C. N., Blanc, M., Lerat, S., Jagu, A., Coquio, T. (2025). Centrifuge modelling of intermediate piles subjected to multidirectional cyclic lateral loading. In Proceedings of the 5th International Symposium on Frontiers in Offshore Geotechnics (ISFOG 2025). Nantes, France. https://doi.org/10.53243/ISFOG2025-318.

Zhang, Y., Andersen, K.H., Jeanjean, P., 2020. Verification of a framework for cyclic p-y curves in clay by hindcast of sabine river, solcyp and centrifuge laterally loaded pile tests. *Applied Ocean Research* 97, 102085. doi:10.1016/j.apor.2020.102085.